

Article

Probe Diagnostics and Optical Emission Spectroscopy of Wave Plasma Source Exhaust

Andrei I. Shumeiko ^{1,2} , Viktor D. Telekh ²  and Sergei V. Ryzhkov ^{3,*} ¹ Advanced Propulsion Systems LLC, Nobel Street 7, 2/35/5, Skolkovo, 121205 Moscow, Russia² Department of Plasma Power Plants, Bauman Moscow State Technical University, 2 Baumanskaya Street 5, 1, 105005 Moscow, Russia³ Department of Thermal Physics, Bauman Moscow State Technical University, 2 Baumanskaya Street 5, 1, 105005 Moscow, Russia

* Correspondence: svryzhkov@bmstu.ru

Abstract: Wave plasma sources (WPSs) were first proposed in the 1970s for electric propulsion (EP), and these research and development processes culminated in the flight test in 2021 of the WPS-based thruster REGULUS. Recently, new approaches to WPS use have emerged—multiple schemes of EPs that can generate propelling forces in multiple directions within a single thruster head, regarded as a breakthrough technology for in-space propulsion systems (PSs). One of the concepts is the bi-directional wave plasma thruster that is based on the open-ended gas discharge chamber—the symmetrical system. Up to now, the WPSs based on the open-ended chambers have not been widely studied. In this paper, the plasma flow formed by the WPS based on the open-ended chamber was axially characterized using a retarding potential analyzer (RPA), Langmuir probe (LP), and optical emission spectroscopy (OES). The presence of the double-layer (DL) was confirmed by a drastic change in the plasma potential along the axis, and a specific impulse of 1100 s was indirectly measured. The measurement results show the potential of the WPS based on the open-ended chamber for efficient operations.



Citation: Shumeiko, A.I.; Telekh, V.D.; Ryzhkov, S.V. Probe Diagnostics and Optical Emission Spectroscopy of Wave Plasma Source Exhaust. *Symmetry* **2022**, *14*, 1983. <https://doi.org/10.3390/sym14101983>

Academic Editors: Fabio Sattin and Eugene Oks

Received: 29 July 2022

Accepted: 19 September 2022

Published: 22 September 2022

Publisher's Note: MDPI stays neutral with regard to jurisdictional claims in published maps and institutional affiliations.



Copyright: © 2022 by the authors. Licensee MDPI, Basel, Switzerland. This article is an open access article distributed under the terms and conditions of the Creative Commons Attribution (CC BY) license (<https://creativecommons.org/licenses/by/4.0/>).

Keywords: plasma source; electric propulsion; propulsion systems; thruster; multiple thrust vectoring; spacecraft; probe diagnostics; optical emission spectroscopy; bi-directional thruster

1. Introduction

Nowadays, EP thrusters are becoming an intrinsic part of every space mission. EP thrusters are proposed to be used for multiple in-space applications ranging from attitude control to orbit alterations and interplanetary flights [1–4].

Among EPs, the most elaborated thrusters are Hall-effect, ion, and electrospray thrusters [5–8]. These types of thrusters can be classified as conventional EP. Hall-effect, ion, and electrospray thrusters have achieved the most mature state and have a rich flight heritage thanks to decades of research and development. In addition, a burst of research, development, and in-space use has been observed regarding the monopropellant thrusters.

Despite the high technology readiness level of the conventional EPs and some other PSs, within the advancement of the space missions, EPs and PSs, in general, are becoming more and more limited in their capabilities to satisfy the new requirements—miniaturization, performance enhancement per unit of mass, volume and power, a lifetime in aggressive ambient conditions and at high power, and a broad range of thrust and specific impulse alterations [9,10]. The latter issue with the conventional PS—the achievement of the thruster's capability of creating propulsive forces in multiple directions—has been solved in different ways during the decades of research. Configurations of the cold gas, monopropellant rocket engines, laser ablation thrusters (LAT), FEED, including the recently designed ENPULSION thruster, pulsed plasma thrusters (PPT), and mechanical PSs were proposed to provide multiple thrust vectoring capability to some extent. Furthermore,

gimbaled Hall-effect and ion thrusters—for example, developed by BUSEK Co. Inc.—can be capable of creating thrust vectors in multiple directions. However, conventional PSs with multiple thrust vectoring capability have relatively notable drawbacks. Cold gas and monopropellant rocket engines have a low total impulse. LAT, FEEP, and PPT have a low thrust. Gimbaled Hall-effect and ion thrusters have high levels of complexity and the risk of mechanical parts' failure, and mechanical PSs need desaturation or are incapable of operating without the presence of an external magnetic field.

Some studies have targeted new approaches in creating propulsive forces in multiple directions within a single device in space because it is not often possible to achieve the requirements for satisfying the needs of modern space missions using conventional EP thrusters [4,10–12]. In recent research, electrodeless plasma generation and control have been considered to be promising.

WPS is one of the types of plasma sources based on electrodeless technologies. WPS is scalable because it can be operated in multiple power regimes thanks to the several plasma acceleration mechanisms they can perform. In addition, WPS can be used in harsh ambient conditions. Moreover, based on this technology, it is possible to create EP with the multiple thrust vectoring capability. However, the wave plasma sources are still in a middle development stage—despite the REGULUS thruster based on this technology having a flight test [13]—yet the evidence of their high-performance capabilities has not been widely verified [14–16]. Nevertheless, the possible advances—especially the multiple thrust vectoring capability that the WPS can provide—have attracted attention and pushed its further development.

In this paper, in Section 2, the general principles of the WPS's operations and problems are discussed. In Section 3, the experimental setup for studying the WPS exhaust is overviewed. In Section 4, the results of the experiments are presented. The conclusions are in Section 5.

2. Wave Plasma Sources

The WPS can be considered to consist of two stages—the plasma generation and acceleration stages (Figure 1). However, these two stages are not distinct and separate and are integral parts of each other. In this work, the high-frequency (HF)- and radiofrequency (RF)-based WPS sources are discussed.

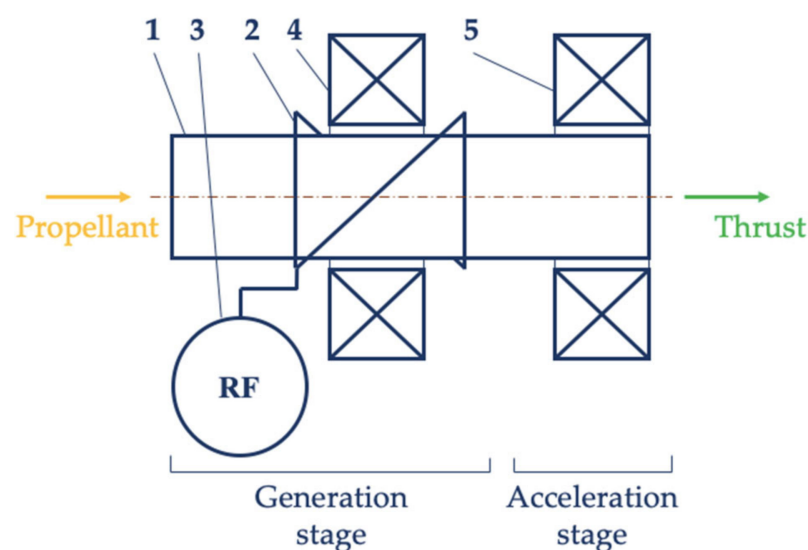


Figure 1. Wave plasma source principle scheme: 1—the gas discharge chamber; 2—the antenna; 3—the RF generator; 4—the magnetic system; 5—the magnetic nozzle.

2.1. Plasma Generation Stage

The plasma generation stage usually constitutes a gas discharge chamber, an antenna, and a magnetic system. The gas discharge chamber used predominantly has been a cylindrical tube, but the close ring-shaped gas discharge chamber has recently been proposed [12]. Multiple types of antennae have been proposed for over five decades. However, the most common type of antenna is the one-half helical.

The antenna generates the alternating electromagnetic field inside the gas discharge chamber. Plasma is generated and sustained by the alternating electromagnetic field created by the antenna. Initially, free electrons presented in every medium gain energy from the field, and after achieving the ionization potential of the propellant supplied into the source, ionize the particles. After ionization, the field transfers its energy to electrons in the plasma.

The magnetic system creates a direct current (DC) magnetic field that should be parallel to the antenna axis. The axial DC magnetic field externally applied to the plasma in the gas discharge chamber creates the conditions for the wave's excitation in the plasma bulk.

The type of excited wave depends on multiple parameters—mainly on the frequency of the alternating current (AC) applied to the antenna, the externally applied DC magnetic field magnitude, and the type of the antenna. A WPS may be classified as an ion cyclotron resonance (ICR) source, a direct fusion drive (DFD) source, a helicon plasma (HP) source, and an electron cyclotron resonance (ECR) source based on the excited waves. ICR and DFD sources generate left-hand polarized waves and operate near ICR and lower hybrid frequencies, respectively. ECR and HP sources generate right-hand polarized waves and operate at ECR and between the ICR and ECR frequencies, respectively. It should be noted that in the last decades, since the antenna most in use in WPS for EP was one-half helical, the waves that were broadly investigated were helicon waves. In general, antennae can be supplied not only by the electric source generating RF currents, as it is supposed in the aforementioned paragraphs, but also by electric currents with frequencies lower than 1 MHz. In this work, microwave sources are not considered. The supply of the antenna with currents of high frequency (HF)—up to 1 MHz—has scientific and engineering rationale. In WPS, utilizing the RF-supplied antennae, the alternating electromagnetic field created by the antenna can propagate into the surrounding—parts of the thruster or PS—or sputter the antenna's external surface causing within some time degradation of the thruster characteristics, decreasing the lifetime of the EP, and at some moment causing system failure. The problems with RF antennae are discussed in some research [12,17]. The negative drawbacks of the RF antennae are caused by the capacitive coupling of the RF antennae with the surroundings.

At relatively low RF powers, the WPS operates in the capacitive coupling plasma (CCP) mode inside the gas discharge chamber—the same as the conventional inductively coupled plasma (ICP) sources do. Similarly to ICP sources, WPS also exhibits parasitic discharges around the antenna. As the RF power supplied to the antenna increases, the discharge inside the gas discharge chamber moves from the CCP to ICP modes and then to the wave mode—in the simple case, hysteresis effects on RF plasmas in the presence of external magnetic fields are not taken into account [18]. However, the parasitic discharge occurrence around the coupler—the antenna—does not transit to the other mode or disappear. Instead, the CCP around the coupler intensifies. The result of capacitive coupling between the coupler and the surroundings—the vacuum chamber walls—is presented in Figure 2, where it can be seen that the whole vacuum chamber volume discharges.

The solution preventing the effects of the CCP around the antenna has been proposed in the works of Shumeiko et al. [12] and Takahashi [17]—the antenna can be surrounded by a metallic shield and ceramic material. However, the shielding of the antenna by these additional means can lead to the deterioration of the thruster's characteristics—for example, a decrease in the specific thrust, specific impulse, and power per unit of mass and volume. Nevertheless, in some studies, multiple concepts of EP that do not suffer from the CCP occurrence around the coupler have been proposed [19]. The proposed EPs comprise the HF antenna. The HF antenna may eliminate drawbacks of the RF antenna regarding the

electromagnetic effects on the external surface of the antenna or the other parts of the EP and spacecraft. The HF antenna—or the magnetically-enhanced antenna—consists of conductive material and a magnetic core (see Figure 3). However, the efficiency and practical applications of the EP with the magnetically-enhanced antennae have not been shown yet [20].

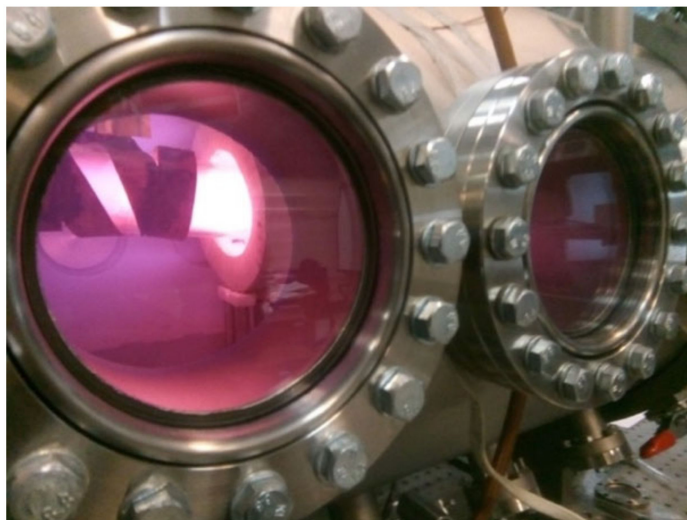


Figure 2. Capacitive coupling volume effect. Inside the vacuum chamber is the testing of the WPS HPT-50 at Bauman University.

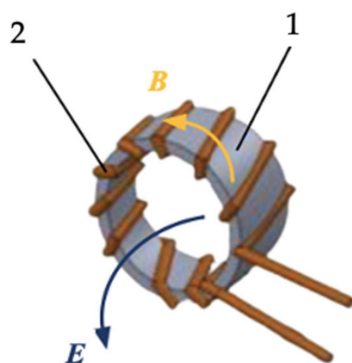


Figure 3. Magnetic (B) and electric (E) fields created by magnetically-enhanced antenna: 1—magnetic core; 2—conductive material.

2.2. Plasma Acceleration Stage

In the conventional WPS, the acceleration stage is the magnetic nozzle. To date, magnetic nozzles have been either permanent magnets, solenoids, or systems consisting of multiple solenoids. The acceleration mechanisms that can be implemented by the magnetic nozzles are electrostatic (double-layer formation), electromagnetic, thermal (plasma is heated up to very high temperatures that increase the kinetic energy of ions), and gas dynamic (the magnetic nozzle should have the geometry of the magnetic lines similarly to the Laval nozzle. The formation of the double-layer is of interest for the low-power electrodeless plasma thrusters. The acceleration in the double-layer occurs because the volume negative charge at the expanding region of the magnetic nozzle is formed. The volume accelerates the positive ions.

The use of the permanent magnets as the magnetic nozzles has a main advantage over the solenoids—saving the power supplied to the thruster. On the other hand, solenoids

provide more adjustability of the plasma flow control—and the corresponding thruster characteristics control—than permanent magnets.

Noting the capabilities of the thrusters based on the WPS for creating propulsive forces in multiple directions, the simple magnetic nozzles do not fit the expectations of providing multiple thrust vectoring capabilities [4]. Nevertheless, these capabilities may be provided by the magnetic nozzles with the alteration in the magnetic field lines' directions and the corresponding alteration of the thrust vector because the plasma flow that is responsible for the thrust force generation follows magnetic field lines—in case the electrons are magnetized by the field created by the magnetic nozzles (see Figure 4).

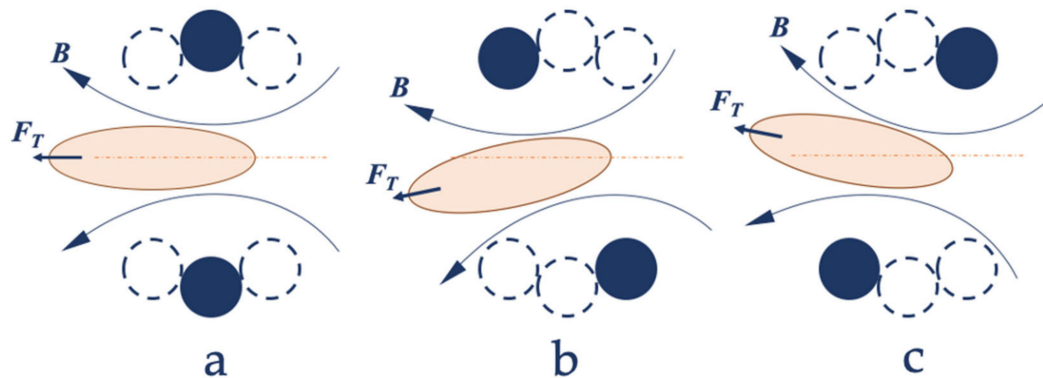


Figure 4. Wave plasma source principle scheme: (a)—the magnetic field lines co-directional with the gas discharge chamber axis; (b)—the magnetic field lines inclined at the arbitrary position to the gas discharge chamber axis; (c)—the magnetic field lines inclined at the other arbitrary position to the gas discharge chamber axis.

In addition, enhancement of the magnetic nozzle operations may occur when the two solenoids constituting the magnetic nozzle have currents in different directions. One of the solenoids will create the convergent field from the upstream side to trap the plasma flow from the plasma generation stage, and the other solenoid will cut the infinitely divergent part of the first solenoid to prevent the creation of the magnetic lens. The magnetic field within this approach drastically expands and is still self-closed. Thus, the plasma flow will be collimated, the losses of the ions inclined by the magnetic lens in the directions that are not the axis of the required thrust vector will be decreased, and the specific thrust per unit of power, mass, and volume can be increased.

3. Experimental Setup

3.1. Testing Facility

The experiments were conducted in a vacuum chamber made of nonmagnetic stainless steel. The vacuum chamber is 0.7 m in diameter and 1 m long. The pumping station—Pfeiffer HiCube 300—is connected to one of the flanges of the gas discharge chamber. The pumping station is capable of maintaining the dynamic pressure of 5 mTorr, while the mass flow rate of the Ar supplied to the vacuum chamber is 1.5 mg/s. The MKS 220CA Baratron gauge was used for pressure measurements in the vacuum chamber. The controller MKS 2160B was used to control the mass flow rate of the propellant.

For the supply of the WPS, the RF generator AE Cesar 1000TM was used. The matching network for the adjusting impedance of the RF generator and the WPS antenna was AE NavioTM digital matching network. The frequency of the RF current supplied to the antenna was 13.56 MHz.

3.2. Wave Plasma Source WPS-20

The laboratory model of the WPS consists of a gas discharge chamber of 200 mm long. The gas discharge chamber has an inner diameter of 16 mm with a wall thickness of 2 mm (see Figure 5). In the central part of the gas discharge chamber from the outer surface side,

the one-half helical antenna made of silver and palladium is located—the palladium is used for the enhancement of the construction characteristics of the antenna. The length of the antenna is 40 mm, the inner diameter is 22 mm, and the outer diameter is 26 mm. Between the gas discharge chamber's outer surface and the antenna's inner surface, there is a gap of 1 mm for the prevention of contact between the gas discharge chamber and the antenna due to the thermal expansion of the source's parts during the source operations. The system is symmetrical and only a single end of the gas discharge chamber is studied.

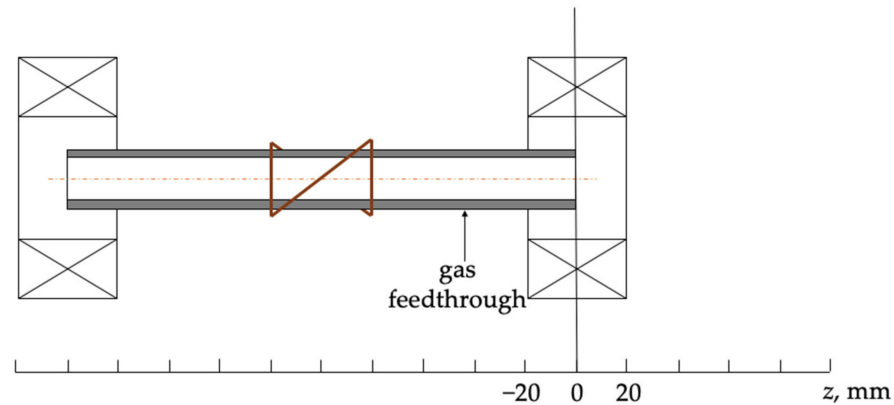


Figure 5. The scheme of the WPS with open-ended gas discharge chamber.

The simple solenoid is located at one of the ends of the gas discharge chamber. The other end of the gas discharge chamber is sealed. The solenoid has a length of 40 mm. The solenoid is capable of creating a magnetic field of around 200 G magnitude—the axial maximum. The magnetic field axial maximum is located at $z = 0$ mm, where z is the axial coordinate. The magnetic field is measured directly by magnetometer. The magnetometer features a sensor that is capable of measuring either transverse or longitudinal magnetic fields. The measurements are conducted when the source is mounted inside the vacuum chamber. During the direct measurements, the magnetometer is mounted on a holder, with which measurements can be carried out with a certain step.

The magnetometer was firmly fixed to the holder with the possibility of step movement. In this case, the accuracy of measured data depended on the accuracy of the magnetometer. According to the magnetometer specification (AlphaLab Inc. GM2, South Salt Lake, UT, USA) the accuracy for DC field is 2%.

The axial distribution of the magnetic field magnitude created by the solenoid and its first derivative are presented in Figures 6 and 7, respectively. The first derivative of the magnetic field magnitude axial distribution is required to determine the probable region of the double-layer. The magnetic field is axially symmetric at $z = 0$.

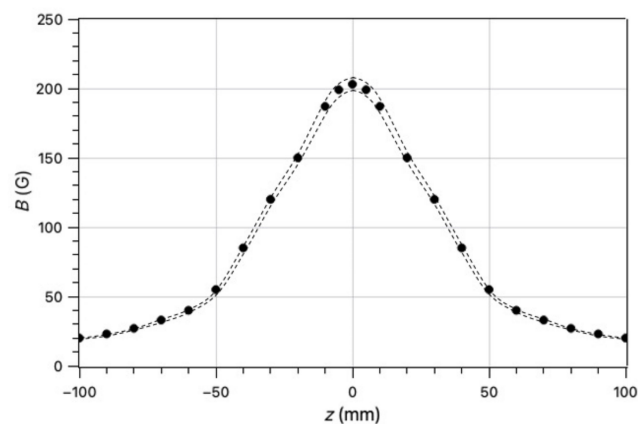


Figure 6. The magnetic field magnitude axial distribution created by the solenoid. The dashed lines denote the measurement accuracy of the magnetometer for each point.

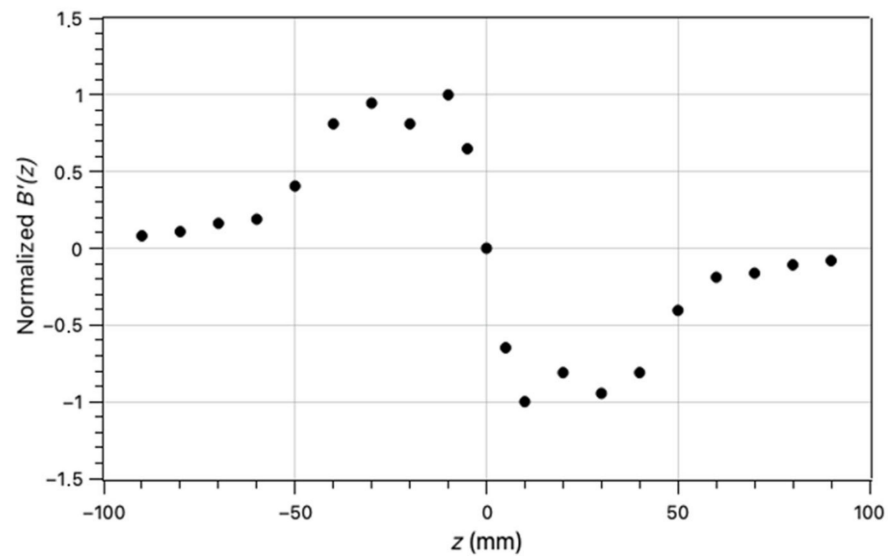


Figure 7. The normalized first derivative of the magnetic field magnitude axial distribution created by the solenoid.

The gas feedthrough is radially connected to the gas discharge chamber at the point 45 mm from the end of the gas discharge chamber where the solenoid is located.

The specifications of the WPS are presented in Table 1.

Table 1. The specifications of the WPS tested.

Parameter	Value
Gas discharge chamber (GDC) length, mm	200
GDC inner diameter, mm	16
GDC wall thickness, mm	2
GDC material	quartz glass
GDC type	open-ended
Antenna type	one-half helical
Antenna length, mm	40
Antenna inner diameter, mm	22
Antenna outer diameter, mm	26
Antenna material	silver and palladium alloy
Number of solenoids	2
Solenoid length, mm	40
Solenoid magnetic field magnitude at I = 2 A, G	200
Solenoid inner diameter, mm	80

The gas feedthrough is radially connected to the gas discharge chamber between the antenna and solenoid for the enhancement of the WPS characteristics. First, the radial propellant supply allows using two sides of the single gas discharge chamber for plasma flow exhausting that allows the creation of minimum propulsive forces in two directions in case the source is used in the EP. Furthermore, the propellant supply location near the acceleration stage increases the specific thrust and specific impulse per unit of power. This phenomenon was observed experimentally by Takahashi et. al. [21] and can be explained theoretically.

The distance within which the energy is absorbed by the plasma is [22]

$$\alpha = \frac{2\omega_{ce}}{k_z v_{eff}} \gg L_{chamber}, \quad (1)$$

where ω_{ce} —is the electron cyclotron resonance that corresponds to the magnitude of the externally applied DC magnetic field, k_z —is the longitudinal wave number, v_{eff} —is the

effective collision frequency, $L_{chamber}$ —the length of the gas discharge chamber that is possible for the WPS operations.

Since the power is absorbed within a certain distance downstream of the antenna, the propellant supplied in the gas discharge chamber between the antenna and the acceleration stage is ionized and absorbs energy with the decreased losses of charged particles on the gas discharge chamber walls because the ionized particles do not pass the long distance between the plasma generation and acceleration stages.

3.3. RPA, Langmuir Probe, and OES

The WPS characteristics are confirmed by the experiments of measurements of the local plasma potential, electron temperature, and ion beam potential to verify the measured plasma characteristics and determine the velocity of the exhausted plasma flow.

The RPA consists of the 3 grids and one plate. The orifice through which plasma ions enter the RPA is 5 mm in aperture. The voltages on the RPA's grids are set to -10 , -20 , and -90 V for the collector plate, secondary grid, and repeller grid, respectively. The voltage applied to the discriminator grid, V_d , that is located between the secondary and repeller grids can be altered from -150 V to 150 V. The RPA allows for the determination of the data for the time-averaged $I - V$ curve from which the ion beam potential, V_{beam} , can be determined.

The Langmuir probe used is RF compensated. The voltage on the bias supply can be altered from -150 to 150 V. The $I - V$ curve is produced from the time-averaged measurements. The Langmuir probe is used to determine the local plasma potential, V_{local} , and the electron temperature, T_e [23]

$$V_f = V_{local} - \frac{k_B T_e}{2e} \ln\left(\frac{2M}{\pi m_e}\right), \quad (2)$$

where V_f —is the floating potential determined from the $I - V$ curve measured by the Langmuir probe, k_B —Boltzmann constant, M —is the mass of the propellant atom, m_e —is the mass of electron.

The electron temperature is determined to verify the measurement data of the Langmuir probe by comparison of T_e measured by the Langmuir probe and the OES. The OES consists of the spectrometer Solar LS S-100 and the lightguide feedthrough into the gas discharge chamber. The light guide is radially placed to the axis of the WPS in the gap between the solenoid and gas discharge chamber. Axial movements are carried out using the mechanical guide into the vacuum camera. The distance between the light guide and the center of the quartz tube is 21 mm.

From multiple models for spectrally obtaining plasma characteristics, the argon collisional-radiative model (CRM) is chosen. The CRM model is constituted by the balance and line intensity equations.

The intensity of a spectral line corresponding to the optical transition from upper level, i , to lower level, j , is [24]

$$I_{ij} = C \frac{hc}{\lambda_{ij}} n_i A_{ij} \eta_{ij}, \quad (3)$$

where η_{ij} —escape factor, A_{ij} —Einstein coefficient, n_i —population density of the excited state, the coefficient C is the same for all lines.

The escape factor can be obtained from the empirical formula introduced by Mewe [25]

$$\eta = \frac{2 - \exp(-10^{-3} k_0 R)}{1 - k_0 R}, \quad (4)$$

where k_0 —absorption coefficient, R —plasma characteristic length.

The absorption coefficient can be determined as [25]

$$k_0 = n_i \frac{g_i}{g_j} \frac{\lambda}{\sqrt{2\pi}} \frac{A}{8\pi} \sqrt{\frac{m_A}{k_B T_g}} \quad (5)$$

where g —statistical weight of state, λ —transition wavelength, T_g —gas temperature, m_A —gas molar mass.

All the processes that occurred at certain level are described by the balance equation. Some of the processes are presented in Table 2.

Table 2. Explanations to the processes included in the model.

Process	Variable	Dependence	References
Diffusion	τ ¹	T_g, p	[26]
Heavy particle ionization	α ²	T_g	[26]
Electron impact (de-)ionization	Q ³	T_e, EEDF ⁵	[27]
Spontaneous emission	Q_{ion}	T_e, EEDF ⁵	[28]
Radiation trapping	A ⁴	-	[29]

¹ τ —diffusion time. ² α —Penning ionization coefficient. ³ Q —rate coefficient. ⁴ A —Einstein coefficient. ⁵ EEDF—electron energy distribution function.

CRM application requires solving a large number of balance equations. In order to facilitate the calculations, only two lines strongly affected by electron temperature are selected. The wavelengths of the ArI lines chosen are $\lambda_{750} = 750$ nm and $\lambda_{811} = 811$ nm. The transition corresponding to λ_{750} line is from $4p[5/2]_3$ to $4s[3/2]_2$. The transition corresponding to λ_{811} line is from $4p'[1/2]_0$ to $4s[1/2]_1$.

The result of the ratio of balance equations for the lines chosen with the implementation of Equation (3) is

$$\frac{I_{811}}{I_{750}} = b \left(\frac{Q_{gs \rightarrow 4p[5/2]_3}}{Q_{gs \rightarrow 4p'[1/2]_0}} + \frac{n_{4s[3/2]_2}}{n_{gs}} * \frac{Q_{4s[3/2]_2 \rightarrow 4p[5/2]_3}}{Q_{4s[3/2]_2 \rightarrow 4p'[1/2]_0}} \right) \quad (6)$$

where b is found to minimize the error function between the calculated and measured intensity ratios.

In order to evaluate $\frac{n_{4s[3/2]_2}}{n_{gs}}$, the equation given [30] is used. The rate coefficient, Q , can be determined as

$$Q(T_e, x, E_{max}) = \frac{1}{n_e} \int_0^{E_{max}} \sigma(E) v f(T_e, x, E) dE. \quad (7)$$

Cross-sections $\sigma(E)$ are given by [31].

The relation (6) depends on the electron temperature. Thus, the electron temperature can be calculated from the data regarding the lines' intensity ration at certain position.

4. Results

The measurements were conducted under the following conditions: the magnetic nozzle magnetic field magnitude was 200 G, the forwarded RF power in plasma was 90 W, the Argon flow rate was $1.5 \text{ mg} \cdot \text{s}^{-1}$, and the pressure in the vacuum chamber was 5 mTorr. The measurement error limits during the experiments were $\pm 5\%$.

The experiments aimed at measuring the plasma characteristics to determine the velocity of the exhausted plasma flow. The measurements were conducted on the centerline of the WPS. First, the electron temperature, T_e , was determined from the $I - V$ curve obtained from measurements by LP. The power source by which the voltage to the Langmuir

probe was applied was electronic with the accuracy of 1%. The values of current for each point were measured 30 times. The median value of these 30 measurements was found. The accuracy interval of the median located was the max and min of the measured values. The accuracy interval for each point did not exceed 5% of the median value.

One of the $I - V$ curves—the curve measured in the probable region of the double-layer presence, $z = 8.5$ mm—is shown in Figure 8.

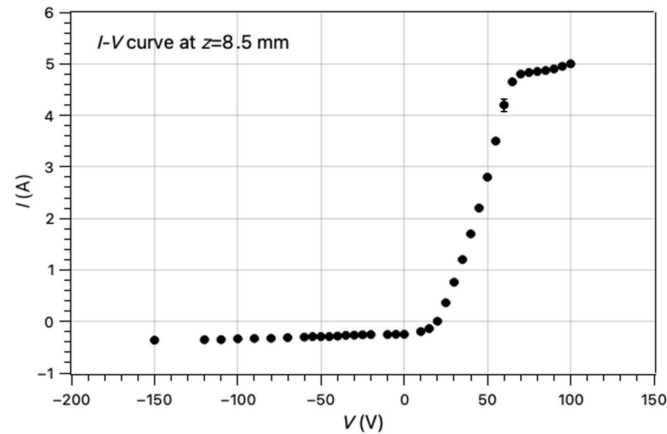


Figure 8. The $I - V$ curve obtained from measurements by LP in the probable region of the double-layer presence, $z = 8.5$ mm. The accuracy intervals of 5% of current value can be applied to each point. As an example, the accuracy interval for the point at $V = 60$ V is shown.

The measurement results of the LP were verified by the comparison of data regarding T_e obtained by LP and OES. For the electron temperature, the data were based on the measured $I - V$ curves. Since for the calculation of the electron temperature from the data measured by the Langmuir probe diagnostics the physics constant values are used, for example, Boltzmann constant, the accuracy of the data calculated is limited to the accuracy of the data measured. Hence, the accuracy of the values calculated lies in the interval of 5% of the value at each point. For the electron temperature measured by the OES, the minimum error between the measured values and calculated values was achieved. The error bars were not set for the values since the data were in good correspondence with the Langmuir probe measurements.

The results on T_e measured by the LP and OES at different axial positions are presented in Figure 9. From Figure 9, it can be concluded that at position $z = 8.5$ mm, the plasma flow may experience an expansion due to the drastic decrease in the electron temperature.

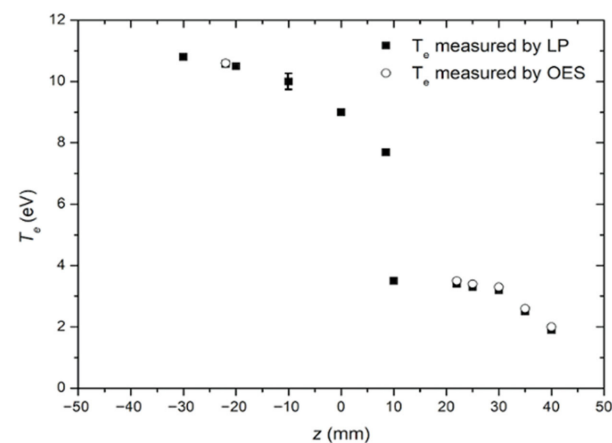


Figure 9. The results on T_e measured by the LP and OES at different axial positions. The accuracy intervals of 5% of current value can be applied to each point. As an example, the accuracy interval for the point at $z = 10$ mm is shown.

Then, the axial ion energy distribution function (IEDF) is calculated from RPA measurements. The power sources by which the voltage to the RPA electrodes was applied were electronic with the accuracy of 1%. The values of current for each point were measured 30 times, the same as for the Langmuir probe measurements. The mean value of these 30 measurements was found. The accuracy interval of the mean located was the max and min of the measured values. The accuracy interval for each point did not exceed 5% of the mean value. The measurement results at $z = 8.5$ are shown in Figure 10. The maximum cut-off energy in the axial IEDF is about 110 V.

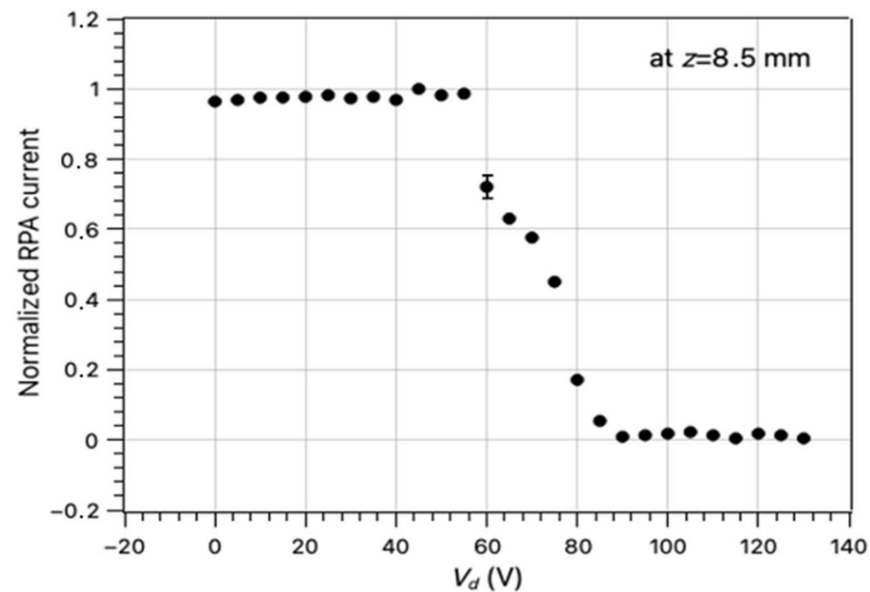


Figure 10. The axial IEDF at $z = 8.5$ mm. The accuracy intervals of 5% of current value can be applied to each point. As an example, the accuracy interval for the point at $V = 60$ V is shown.

From the normalized IEDF, V_{beam} is determined for each axial position—see Figure 11 for the normalized IEDF at $z = 8.5$ mm. The line exhibits two peaks corresponding to the local plasma potential ($V_{local} \sim 60$ V) and to the ion beam ($V_{beam} \sim 80$ V).

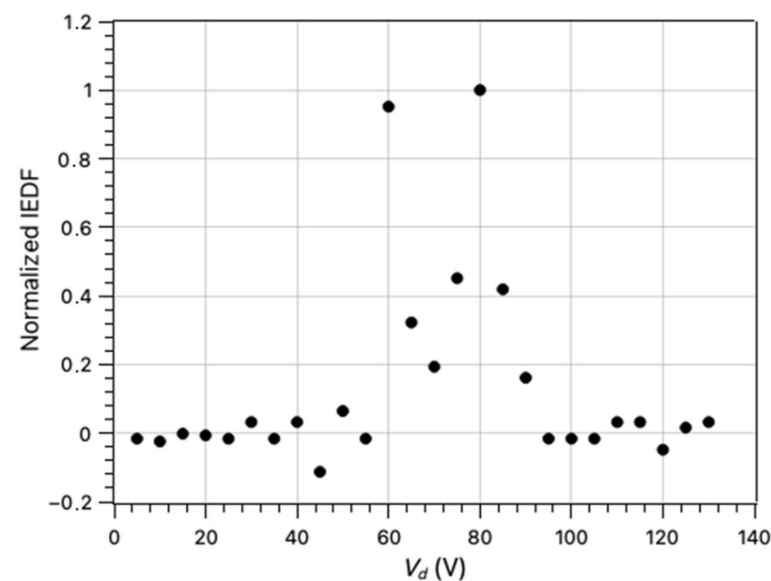


Figure 11. The normalized IEDF at $z = 8.5$ mm.

After the verification of the LP measurement results, V_{local} downstream of the solenoid of the WPS was measured at several axial positions. The V_{local} and V_{beam} were determined from the $I - V$ curves and normalized IEDF respectively. The accuracy for the $I - V$ and IEDF was about 5%. Hence, the accuracy of the V_{local} and V_{beam} is the same since the physical constants are used for its determination, for the case of V_{local} , or the value is determined from the plot, for the case of V_{beam} .

The measurement results on the V_{local} and V_{beam} at different axial positions are shown in Figure 12.

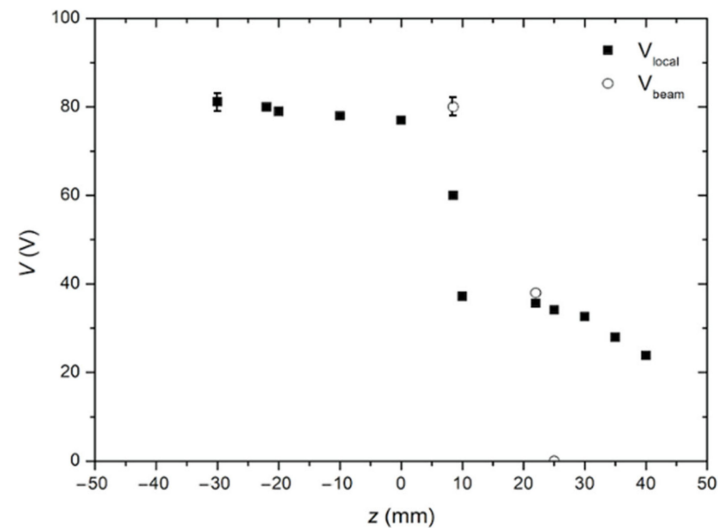


Figure 12. The measurement results on the V_{local} and V_{beam} at different axial positions. The accuracy intervals of 5% of current value can be applied to each point. As an example, in the case of V_{local} , the accuracy interval for the point at $z = -30$ mm is shown, in the case of V_{beam} , the accuracy interval for the point at $z = 8.5$ mm is shown.

From Figure 12, the presence of the double-layer at $z = 8.5$ mm is confirmed by a drastic change in the plasma potential along the axis. Then, the velocity of the exhausted plasma beam at $z = 8.5$ mm is determined from the data regarding V_{local} and V_{beam} using the following equation [16]

$$v_{beam} = \left(\frac{2e(V_{beam} - V_{local})}{M} \right)^{1/2}. \quad (8)$$

The plasma beam velocity obtained is $11 \text{ km} \cdot \text{s}^{-1}$.

Generally, the plasma flow—ions—acceleration in WPS occurs due to several mechanisms that are electrostatic (double-layer formation), electromagnetic, thermal (plasma is heated up to very high temperatures that increase the kinetic energy of ions), and gas dynamic (the magnetic nozzle should have the geometry of the magnetic lines similarly to the Laval nozzle. In this paper, the low-power WPS is considered and the dominant mechanism of plasma acceleration is electrostatic, implemented by the formation of the double-layer. It is important to indirectly measure the velocity of ions in the region where the acceleration occurred—at $z = 8.5$ mm—because downstream from this region the processes of deionization take place, and the results of the measurements may not be reliable. The smaller difference between V_{local} and V_{beam} downstream—for example, at $z = 20$ mm—does not mean a decrease in the velocity. It only means that the density of charged particles decreased, and the flow consisted of neutral particles. Thus, to measure the velocity of particles downstream from the acceleration region, different techniques should be applied.

5. Discussion and Conclusions

The testing of the wave plasma source WPS-20 was aimed at obtaining verified data regarding one of the critical characteristics for EP—the velocity of the exhausted plasma beam. This characteristic is one of the responsible parameters for the efficiency of EP. From the experimental and calculated results, the velocity of the exhausted plasma beam is $11 \text{ km}\cdot\text{s}^{-1}$ at the gas flow rate of $1.5 \text{ mg}\cdot\text{s}^{-1}$, and the power in the plasma is 90 W. The measured and determined plasma beam velocity of the WPS-20 allows for its selection as the source of the base technology for further development of the electrodeless EP; more specifically, for the development of the EP with multiple thrust vectoring capability. Moreover, the WPS-20 source is considered to have been tested in mixes of the gases simulating the ambient conditions in low Earth orbits (LEO) to determine the lifetime.

Despite the relatively high measured velocity of the exhausted plasma beam from the source, there are still some issues with the power efficiency that limit the velocity and make the WPS less appealing in comparison to the conventional EP—the Hall-effect, ion, and electrospray thrusters. Careful studies on the plasma ionization efficiency, antenna-to-plasma power ratio, and complicated magnetic nozzles should be conducted to approach the velocity of the exhausted plasma beam of the WPS to $20 \text{ km}\cdot\text{s}^{-1}$ to be comparable to the conventional EP. Additionally, there are multiple issues that are intrinsic to the WPS. First of all, there is a relatively inefficient energy transfer between the antenna and plasma in the straight-shaped geometries of the gas discharge chambers. Second, the inner walls' surface of the gas discharge chamber may suffer from erosion and sputtering because of the transversal geometry of the electric field of the plasma-induced electromagnetic waves. In addition, there are some issues with WPS's plasma controllability and stability during the alterations in the operational regimes. Nevertheless, the WPS's capabilities of multiple thrust vectoring make the source attractive for further research and development.

Author Contributions: Conceptualization, A.I.S.; methodology, A.I.S.; software, S.V.R.; validation, A.I.S. and V.D.T.; formal analysis, A.I.S.; investigation, A.I.S.; resources, V.D.T.; data curation, A.I.S.; writing—original draft preparation, A.I.S.; writing—review and editing, V.D.T. and S.V.R.; visualization, A.I.S.; supervision, V.D.T.; project administration, A.I.S. and V.D.T.; funding acquisition, V.D.T. All authors have read and agreed to the published version of the manuscript.

Funding: This work was performed using research facilities cluster “Beam-M” of Bauman Moscow State Technical University following the government task by the Ministry of Education and Science of the Russian Federation (0705-2020-0046).

Data Availability Statement: The data presented in this study are available on request from the corresponding author. The data are not publicly available due to interests of Advanced Propulsion Systems LLC.

Conflicts of Interest: The authors declare no conflict of interest.

References

1. Boeuf, J.-P. Tutorial: Physics and modeling of Hall thrusters. *J. Appl. Phys.* **2017**, *121*, 011101. [[CrossRef](#)]
2. Vepa, R.; Shaheed, M.H. Optimal Trajectory Synthesis for Spacecraft Asteroid Rendezvous. *Symmetry* **2021**, *13*, 1403. [[CrossRef](#)]
3. Romadanov, I.; Smolyakov, A.; Raitses, Y.; Kaganovich, I.; Tian, T.; Ryzhkov, S. Structure of nonlocal gradient-drift instabilities in Hall $E \times B$ discharges. *Phys. Plasmas* **2016**, *23*, 122111. [[CrossRef](#)]
4. Shumeiko, A.I.; Jarrar, F.S.; Swei, S.S.M. Development of Novel Electrodeless Plasma Thruster with Multiple Thrust Vectoring Capability. In Proceedings of the International Astronautical Congress 2021, Dubai, United Arab Emirates, 25–29 October 2021.
5. Zakharenkov, L.E.; Semenkin, A.V.; Solodukhin, A.E. Concept of Electric Propulsion Realization for High Power Space Tug. *Prog. Propuls. Phys.* **2016**, *8*, 165–180. [[CrossRef](#)]
6. Shilov, S.; Ivakhnenko, S.; Vorob'ev, E.; Manegin, D.; Plokhikh, A.; Vazhenin, N.; Merkurev, D.; Zakharchenko, V. Self-Electromagnetic Emission from a Thruster with Anode Layer Operating with Krypton and Xenon. *J. Phys. Conf. Ser.* **2021**, *1925*, 012081. [[CrossRef](#)]
7. Dale, E.; Jorns, B.; Gallimore, A. Future directions for electric propulsion research. *Aerospace* **2020**, *7*, 120. [[CrossRef](#)]
8. Martynenko, Y.V.; Nagel, M.Y. Electrodynamic plasma thruster with capillary-porous electrode. *Tech. Phys.* **2021**, *66*, 1241–1246. [[CrossRef](#)]

9. Shumeiko, A.I.; Telekh, V.D. Helicon Engine in Outboard Air as a Successful Solution for Maintaining Small Space Vehicle in Orbits up to 200 km. *AIP Conf. Proc.* **2019**, *2171*, 170019. [[CrossRef](#)]
10. Shumeiko, A.I.; Telekh, V.D.; Mayorova, V.I. Development of a Novel Wave Plasma Propulsion Module with Six-Directional Thrust Vectoring Capability. *Acta Astronaut.* **2022**, *191*, 431–437. [[CrossRef](#)]
11. Shumeiko, A.I.; Telekh, V.D.; Mayorova, V.I. Development of a Six-Directional Plasma Propulsion Module for Small Satellites. In Proceedings of the International Astronautical Congress 2020, Virtual, 12–14 October 2020.
12. Shumeiko, A.I.; Jarrar, F.S.; Swei, S.S.M. Advanced Wave Plasma Thruster with Multiple Thrust Vectoring Capability. In Proceedings of the AIAA SciTech Forum 2022, San Diego, CA, USA, 3–7 January 2022. [[CrossRef](#)]
13. Bellomo, N.; Magarotto, M.; Manente, M.; Trezzolani, F.; Mantellato, R.; Cappellini, L.; Paulon, D.; Selmo, A.; Scalzi, D.; Minute, M.; et al. Design and In-orbit Demonstration of REGULUS, an Iodine electric propulsion system. *CEAS Space J.* **2022**, *14*, 79–90. [[CrossRef](#)]
14. Kuzenov, V.V.; Ryzhkov, S.V.; Frolko, P.A. Numerical Simulation of the Coaxial Magneto-Plasma Accelerator and Non-Axisymmetric Radio Frequency Discharge. *J. Phys. Conf. Ser.* **2017**, *830*, 012049. [[CrossRef](#)]
15. Mazouffre, S. Electric Propulsion for Satellites and Spacecraft: Established Technologies and Novel Approaches. *Plasma Sources Sci. Technol.* **2016**, *25*, 0330029. [[CrossRef](#)]
16. Charles, C.; Boswell, R.W. Laboratory Evidence of Supersonic Ion Beam Generated by a Current-Free “Helicon” Double-Layer. *Phys. Plasma.* **2004**, *11*, 1706–1714. [[CrossRef](#)]
17. Takahashi, K. Radiofrequency antenna for suppression of parasitic discharges in a helicon plasma thruster experiment. *Rev. Sci. Instrum.* **2012**, *83*, 083508. [[CrossRef](#)] [[PubMed](#)]
18. Isayama, S.; Shinohara, S.; Hada, T. Review of helicon high-density plasma: Production mechanism and plasma/wave characteristics. *Plasma Fusion Res.* **2018**, *13*, 1101014. [[CrossRef](#)]
19. Godyak, V. Ferromagnetic enhanced inductive plasma sources. *J. Phys. D Appl. Phys.* **2013**, *46*, 283001. [[CrossRef](#)]
20. Lloyd, S.; Shaw, D.M.; Watanabe, M.; Collins, G.J. Ferrite Core Effects in a 13.56 MHz Inductively Coupled Plasma. *Jpn. J. Appl. Phys.* **1999**, *38*, 4275. [[CrossRef](#)]
21. Takahashi, K.; Takao, Y.; Ando, A. Increased thrust-to-power ratio of a stepped-diameter helicon plasma thruster with krypton propellant. *J. Propuls. Power* **2020**, *36*, 961–965. [[CrossRef](#)]
22. Chabert, P.; Braithwaite, N. *Physics of Radio-Frequency Plasmas*; Cambridge University Press: Cambridge, UK, 2011; Chapter 8.
23. Chen, F.F. Langmuir Probe Diagnostics. In Proceedings of the Mini-Course on Plasma Diagnostics, IEEEICOPS Meeting 2003, Jeju, Korea, 2–5 June 2003; pp. 20–111.
24. Gizzatullin, A.R.; Zhelonkin, Y.O.; Voznesenky, E.F.; Gizzatullin, A.R. Application of argon collisional-radiative model for inductive RF discharge research. *J. Phys. Conf. Ser.* **2019**, *1328*, 012025. [[CrossRef](#)]
25. Mewe, R. Relative intensity of helium spectral lines as a function of electron temperature and density. *Br. J. Appl. Phys.* **1967**, *18*, 107–118. [[CrossRef](#)]
26. Iordanova, S.; Koleva, I. Optical emission spectroscopy diagnostics of inductively-driven plasmas in argon gas at low pressures. *Spectrochim. Acta Part B At. Spectrosc.* **2007**, *62*, 344–356. [[CrossRef](#)]
27. Zatsarinny, O.; Bartschat, K. The B-spline R-matrix method for atomic processes: Application to atomic structure, electron collisions and photoionization. *J. Phys. B At. Mol. Opt. Phys.* **2013**, *46*, 112001. [[CrossRef](#)]
28. Vriens, L.; Smeets, A.H.M. Cross-section and rate formulas for electron-impact ionization, excitation, deexcitation, and total depopulation of excited atoms. *Phys. Rev. A* **1980**, *22*, 940. [[CrossRef](#)]
29. Kramida, A.; Ralchenko, Y.; Reader, J. *NIST Atomic Spectra Database, version 5.3*; National Institute of Standards and Technology: Gaithersburg, MD, USA, 2015.
30. Czerwiec, T.; Graves, D.B. Mode transitions in low pressure rare gas cylindrical ICP discharge studied by optical emission spectroscopy. *J. Phys. D Appl. Phys.* **2004**, *37*, 2827–2840. [[CrossRef](#)]
31. Bartschat, K.; Zatsarinny, O.; Bray, I.; Fursa, D.V.; Stelbovics, A.T. On the convergence of close-coupling results for low-energy electron scattering from magnesium. *J. Phys. B At. Mol. Opt. Phys.* **2004**, *37*, 2617–2639. [[CrossRef](#)]